Naval Research Laboratory
Washington, DC 20375-5320

NRL/7320/MR—2023/3

Feature Location and Variability (FLAVAR)

ELIZABETH DOUGLASS

ZHITAO YU

Ocean Dynamics and Prediction Branch
Ocean Sciences Division

DAVID LEWIS

IGOR SHULMAN

Ocean Sensing and Process Branch
Ocean Sciences Division

March 29, 2023

REPORT DOCUMENTATION PAGE

Form Approved
OMB No. 0704-0188

1. REPORT DATE *(DD-MM-YYYY)*	**2. REPORT TYPE**	**3. DATES COVERED** *(From - To)*
29-03-2023	NRL Memorandum Report	10/20 – 10/22

4. TITLE AND SUBTITLE

Feature Location and Variability

5a. CONTRACT NUMBER

5b. GRANT NUMBER

5c. PROGRAM ELEMENT NUMBER

6. AUTHOR(S)

Elizabeth Douglass, Zhitao Yu, David Lewis, and Igor Shulman

5d. PROJECT NUMBER

5e. TASK NUMBER

5f. WORK UNIT NUMBER
6B68

7. PERFORMING ORGANIZATION NAME(S) AND ADDRESS(ES)

Naval Research Laboratory
4555 Overlook Avenue, SW
Washington, DC 20375-5320

8. PERFORMING ORGANIZATION REPORT NUMBER

NRL/7320/MR--2023/3

9. SPONSORING / MONITORING AGENCY NAME(S) AND ADDRESS(ES)

10. SPONSOR / MONITOR'S ACRONYM(S)

11. SPONSOR / MONITOR'S REPORT NUMBER(S)

12. DISTRIBUTION / AVAILABILITY STATEMENT

DISTRIBUTION STATEMENT A: Approved for public release; distribution is unlimited.

13. SUPPLEMENTARY NOTES

14. ABSTRACT

This report presents research conducted during the research project entitled Feature Location and Variability, or FLAVAR. The project had several goals, and the results are presented here. The report focuses on oceanic fronts, or locations where the ocean structure changes significantly over a short distance. These changes are identifiable in temperature, salinity, sea surface height, and sometimes ocean color. Goals of the project included characterizing semi-permanent fronts in the Greenland-Iceland-United Kingtom (GIUK) region of the North Atlantic Ocean and developing an automated tracking algorithm capable of identifying these fronts without human intervention from maps of satellite altimetry or sea surface temperature.

Overall, the project was successful. First, this document will describe the initial efforts to describe and delineate variability of gradients and average location and boundaries of fronts within the GIUK region; the initial analysis of one of these fronts and the aspects of temporal and spatial variability of fronts that can be learned from this analysis. Second, an analysis of how model results are related to spatial variability will be analyzed. Third, the details of a higher-level, more sophisticated approach of a search tree frontal detection approach will be explained, and examples of its use in the GIUK region presented. Finally we discuss the ways in which frontal locations from different variables can be combined to give an integrated frontal location that includes input from all sources (observed and modeled, whether temperature, salinity, sea surface height or ocean color). The results from this project lay the groundwork for development of a robust, operational automated frontal detection system.

15. SUBJECT TERMS

16. SECURITY CLASSIFICATION OF:			**17. LIMITATION OF ABSTRACT**	**18. NUMBER OF PAGES**	**19a. NAME OF RESPONSIBLE PERSON**
					Elizabeth Douglass
a. REPORT	**b. ABSTRACT**	**c. THIS PAGE**	U	32	**19b. TELEPHONE NUMBER** *(include area code)*
U	U	U			(228) 688-4262

This page intentionally left blank.

CONTENTS

This page intentionally left blank.

EXECUTIVE SUMMARY

This report presents research conducted during the research project entitled Feature Location and Variability, or FLAVAR. The project had several goals, and the results are presented here. The report focuses on oceanic fronts, or locations where the ocean structure changes significantly over a short distance. These changes are identifiable in temperature, salinity, sea surface height, and sometimes ocean color. Goals of the project included characterizing semi-permanent fronts in the Greenland-Iceland-United Kingtom (GIUK) region of the North Atlantic Ocean and developing an automated tracking algorithm capable of identifying these fronts without human intervention from maps of satellite altimetry or sea surface temperature.

Overall, the project was successful. First, this document will describe the initial efforts to describe and delineate variability of gradients and average location and boundaries of fronts within the GIUK region; the initial analysis of one of these fronts and the aspects of temporal and spatial variability of fronts that can be learned from this analysis. Second, an analysis of how model results are related to spatial variability will be analyzed. Third, the details of a higher-level, more sophisticated approach of a search tree frontal detection approach will be explained, and examples of its use in the GIUK region presented. Finally we discuss the ways in which frontal locations from different variables can be combined to give an integrated frontal location that includes input from all sources (observed and modeled, whether temperature, salinity, sea surface height or ocean color). The results from this project lay the groundwork for development of a robust, operational automated frontal detection system.

This page intentionally left blank.

FRONTAL VARIABILITY AND LOCATION

1. INTRODUCTION

1.1 Ocean Fronts

Large changes in water temperature or density that occur over short distances are known as ocean fronts. These features are visible in observational data and are often correctly represented in ocean models described as able to resolve mesoscale features. Due to their effects on propagation of sound in the ocean, being able to correctly identify and locate these features is of importance to the Navy. Although some fronts are identified as relatively stable in location, being able to precisely identify them automatically, as opposed to through the efforts of a skilled technician, is an ability that has not yet been developed.

The Feature Location and Variability (FLAVAR) project was intended to develop an algorithm to locate and describe certain semi-permanent oceanic fronts. The algorithm can be applied to satellite data (as available) or to model output, to determine the location of each front on a given day. The analysis presented here is applied to the North Atlantic region known as the Greenland-Iceland-UK (GIUK) Gap, but the process should be applicable to other oceanic regions where semi-permanent fronts have been identified.

The discussion is organized as follows: Section 2 will discuss the methods used for initial analysis of the region, including an assessment of gradient variability and identification of the fronts being discussed. Section 3 will discuss the details of the model runs we did to assess the effects of model resolution on frontal descriptions. Section 4 discusses some details of one of the fronts studied in detail during the analysis. Section 5 discusses the details of the automated front-finding algorithm. Section 6 will discuss an analysis of how to combine different algorithms to produce one results that accounts for multiple oceanic variables. Finally, Section 7 has conclusions and plans for future work.

Manuscript approved March 28, 2023.

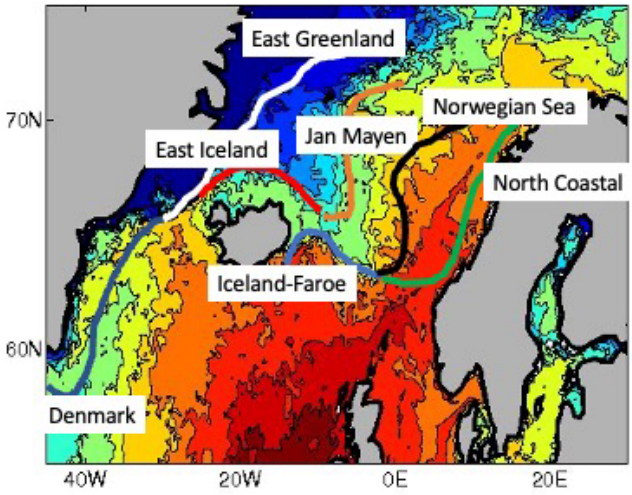

Figure 1 Approximate locations of semi-permanent fronts in the GIUK region, superimposed on model sea surface temperature on March1, 2015.

2. APPROACH

2.1 Model output

For the initial stage of the project, we worked with already-existing model output, rather than develop a new product. The model output used was the GOFS 3.1 reanalysis. This is a model product with nominal resolution of 1/12° at the equator, with 41 vertical levels. As a reanalysis, it was run assimilating the highest quality delayed-mode data and forced with the highest quality wind product. It is our best estimate of "reality" given the observations we have. The model output used was daily means from Jan 1, 2015 to Dec 31, 2015.

2.2 Identification of Fronts

This project is intended to create an algorithm for identifying permanent and semi-permanent fronts. Therefore, the first step is to identify the fronts being examined in the region of interest. Figure 1 shows a schematic of the GIUK region with several fronts labeled, superimposed a sea surface temperature field from the model output on March 1, 2015.

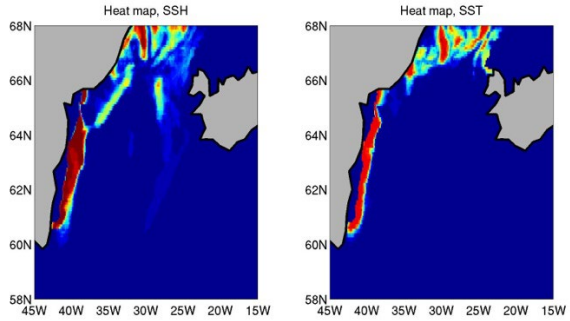

Figure 2 Heat maps for the Denmark Strait Front, along the east coast of Greenland. Colors indicate the number of days in 2015 when each gridpoint was considered to be in a high gradient cluster. Left map is for SSH, right is for SST.

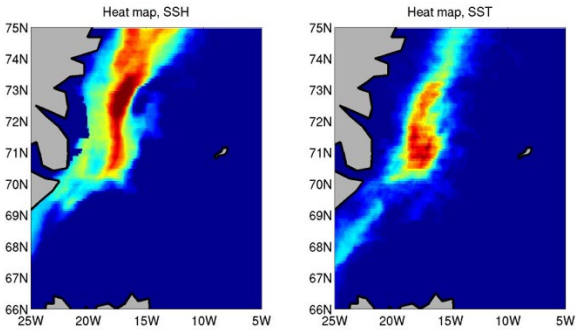

Figure 3 As for Figure 2, but for the East Greenland current (along the northeast coast of Greenland).

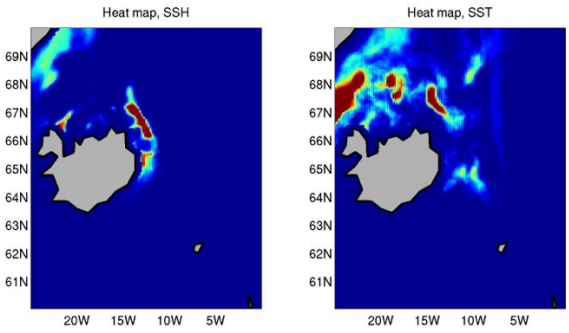

Figure 4 As for Figure 2, but for the East Iceland Front.

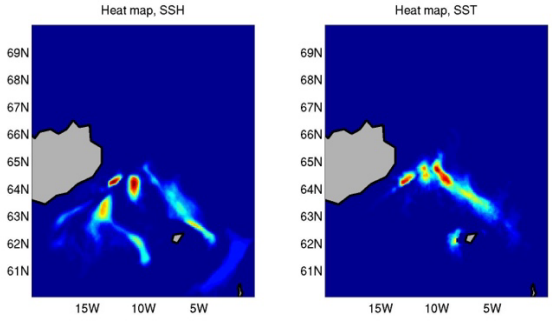

Figure 5 As for Figure 2, but for the Iceland-Faroe Front.

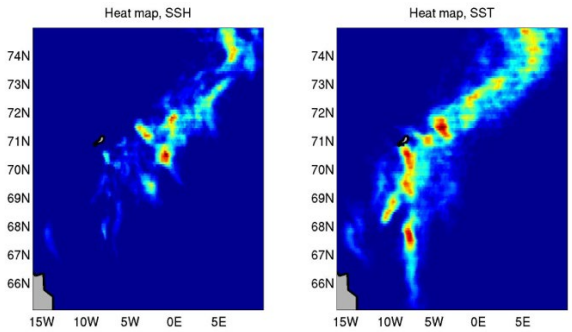

Figure 6 As for Figure 2, but for the Jan Mayen Front.

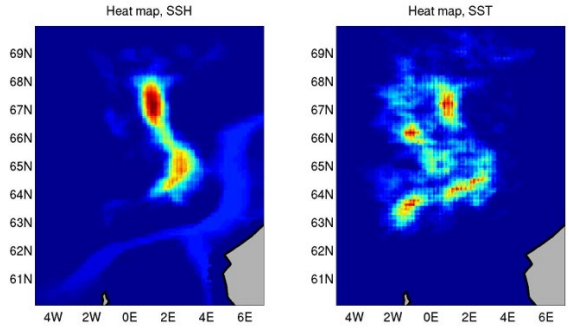

Figure 7 As for Figure 2, but for the Norwegian Sea Front.

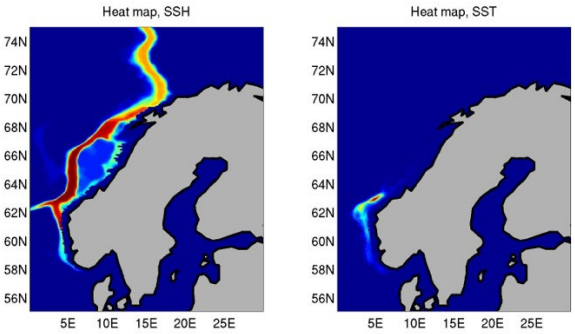

Figure 8 As for Figure 2, but for the Norwegian Coastal Front.

To identify fronts, the spatial gradients of the variable under consideration are calculated. The spatial gradients of sea surface temperature and sea surface height were calculated from the operational model output for the year 2015. Rather than choose a set threshold over which a gradient is considered a front, each location's gradient was considered relative to the mean spatial gradient in a region around the approximate frontal location. If gradient at a location was more than one standard deviation above the spatially averaged gradient, it was considered "high". However, simply having a point of high gradient was also not enough for a location to be considered a front. Frontal locations require not only one point of high gradient, but a cluster of such point; thus, for each point of high gradient, a box of 3x3 gridpoints was considered, and the number of those points with high gradient were counted. If all nine points in this 3x3 box had high gradients, then the location was flagged as a possible frontal location. This calculation was performed for each gridpoint in the GIUK grid, for each day of 2015. Figs 2a and 2b show the number of days in 2015 when each gridpoint was flagged as a frontal location, for SSH and SST respectively, in the region near the Denmark Strait Front. This map will be referred to as a "heat map." It essentially depicts the probability that a given gridpoint will be within a cluster of high gradient at some point during the year.

The heat maps reveal several important things about the fronts. First, they show that while each front has some locations where fronts are consistently very strong, they also have weaker locations, and it becomes clear that the challenge here is drawing a connected line between those stronger locations, connecting the locations with obviously high gradients through locations where the specific path of the front is less clear. Second, the locations of the SST and SSH signals are not always the same. In the Jan Mayen Front, the SST map indicates more than one pathway for the front, while the SSH map has one path. On the other hand, the Iceland-Faroe front seems to show a southern "branch" in the SSH map that is not evident in the SST field. Determining the location of the "correct" front is complicated in such cases. Third, the strengths of the SST and SSH signals can be vastly different. The Norwegian Coastal front (Fig. 8) is an obvious example of this, as the SSH heat map shows a very strong, compact, consistent front. The SST heat maps shows nearly nothing, indicating that this front does not have a strong temperature signature. It likely indicates a strong coastal current guided by topography; it is nonetheless important, and it is clear that the best way to identify it is using sea surface height rather than temperature.

These heat maps, while somewhat qualitative rather than quantitative, provide some direction for the next step in determining frontal location. They give in each case a rough depiction of the shape of the front, and can be used to define an "envelope" for each front within which all expected frontal locations will fall. This will be one of the starting points for frontal determination. Additionally, they illustrate which of these two parameters will be more useful in finding a clear connected frontal location. SSH is the most appropriate measurement for locating the NC front, while SST will be more helpful for the Jan Mayen. Several fronts are well represented in both, and will provide a testbed for determining the interaction of SST and SSH and how they are related to subsurface frontal structure.

3. ICELAND-FAROE FRONT

3.1 Mean Structure

From the seven fronts shown in the schematic in Fig 1, the Iceland-Faroe was chosen as the initial front analyzed in detail. It was chosen as a front that is evident in both SSH and SST observations, but may still present some difficulties as it is not always in precisely the same location or with the same intensity. As such it presents a good location to test methods for dealing with such inconsistencies, which is important in developing a robust algorithm.

A first step in this process is calculating the mean front, estimated from the heat maps. This is shown in Fig. 9.

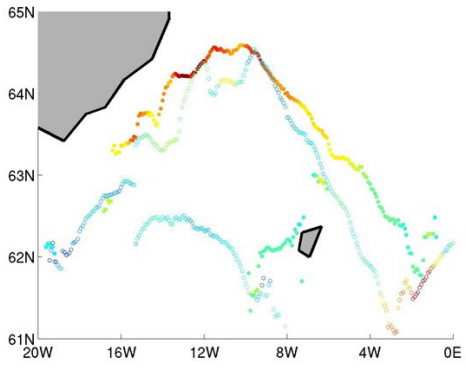

Figure 9 Time-mean of location and magnitude of Iceland-Faroe Front in SST (closed circles) and SSH (open circles).

In this figure, since SST and SSH gradients have very different magnitudes, each is normalized relative to their own local maximum. The figure demonstrates a few things about this front. First of all, there is a

"southern branch" (near 62N between 16W and 10W) evident in both SST (closed circles) and SSH (open circles). Examination of local topography shows that this "branch" is south of a ridge running between Greenland and Iceland. The southern branch is less persistent and weaker in magnitude so will generally be ignored; however, knowing it's there sometimes is useful information; it forms part of the climatology of the front in this region that can inform decisions. In both SSH and SST, the northern peak of the front is at about 10W and 65N; this is also the region in which the SST gradients are at their highest (red color). SSH gradients, on the other hand, peak far to the east, closer to 2W. Additionally, in the eastern part of the front, it is clear that SST and SSH diverge, with the SST front running significantly farther north than the SSH front. This is indicative of a systematic subsurface structure causing the SSH signature (which is an integrated measurement of full-depth frontal location) to be misaligned with SST frontal location (which is the immediate surface measurement only).

3.2 Time Variability

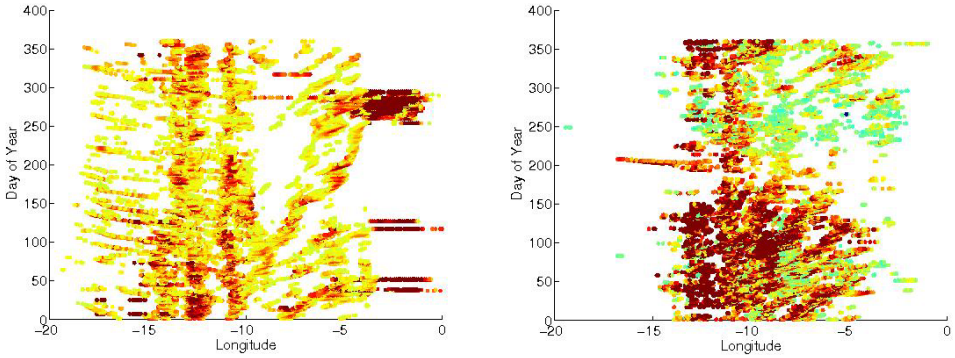

Figure 10 Maximum gradient of SSH (left) and SST (right) as a function of longitude and time.

An examination of the location of maximum gradient in the Iceland-Faroe front led to discovery of an interesting phenomenon. For each day, for gradient "clusters" with gradients above an ad hoc threshold, the magnitude of gradient was plotted as a function of longitude. This is shown in Figure 10. What emerges in this Hovmoller diagram is a situation in which high-magnitude gradients are propagating eastward along the front in time. These diagonal lines are present in both SSH gradients and SST gradients. There are more, perhaps 3 or 4, starting near 10W (the peak of the fronts) in the first few months of the year, extending to roughly 5W over the course of about two months. In the last half of the year this phenomenon is less frequent and less prominent. .In order to better visualize this phenomenon, for each day, the location of maximum gradient magnitude was plotted in its lat-lon location for a one-month period from day 85-115 (March 25-April 15). It is evident in both SST and SSH that the maximum gradient is propagating eastward and southward along the front as time elapses.

What is the source of this propagation? In order to examine this phenomenon we examine maps of SST and SSH evolution. In each map, there is a clear front between high temperature and SSH in the south/west and low temperature and SSH in the north/east. On March 28, there is a small meander toward the north/west of the front, where the warm southern water pushes against the cooler northern water and the gradient is higher than usual; a small meander in the frontal pathway. This meander travels down the front, pushing higher gradients as it travels, and creating the phenomenon seen in Figure 11. It is shown again on April 20, as it reaches the lowest point of the front, at which point it dissipates. From this analysis, we can deduce that meanders that travel along the pathway are a feature of the Iceland-Faroe front. Understanding and identifying phenomena like these will help to identify the state a given front is in and even predict the ways in which it might evolve.

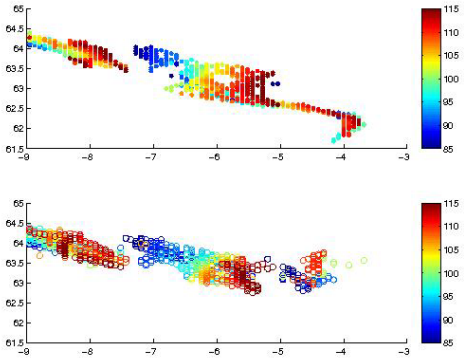

Figure 11 Location of maximum gradient from days 85-115, colored by time. This demonstrates that the maximum gradient progresses down the front.

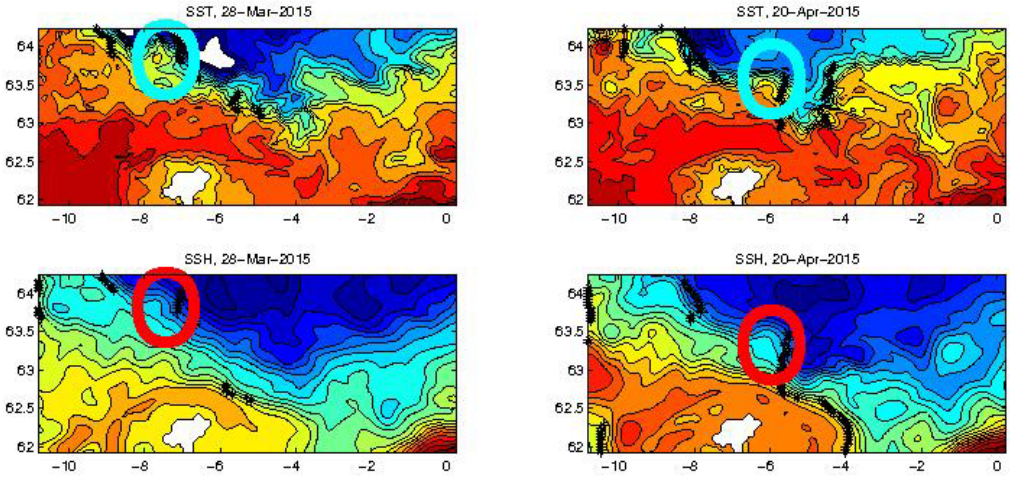

Figure 12 Maps of SST and SSH for days 88 and 101. Black stars show locations of high gradient. Circles show the meander in the path of the front, with high gradients just east of the meander.

4. MODELING

4.1 HYCOM

In order to analyze the effects of resolution on the representation of fronts in the GIUK region, several model simulations were performed with the HYbrid Coordinate Ocean Model (HYCOM). HYCOM is a primitive equation general ocean circulation model applied to large scale, marginal sea, and coastal studies, and the ocean model component for the present operational US Navy Global Ocean Forecast System (Metzger et al., 2014). HYCOM solves five prognostic equations: two for horizonal velocity components, a mass continuity equation, and two conservative equations that govern temperature and salinity. There are three vertical-coordinate systems coexisting in HYCOM: z-coordinates in unstratified water, sigma-coordinates in shallow depths, and isopycnal coordinates in the stratified ocean. Hence, HYCOM maintains the significant advantages of an isopycnal model in the stratified ocean, but allows coordinate surfaces to locally deviate from isopycnals to provide more vertical resolution near the surface and in shallow coastal regions in order to better represent the upper ocean physics (Chassignet et

al., 2003). With this unique feature, HYCOM serves as a good tool for simulating circulations in the region, which has complex topography that covers the shallow water near the coast to the deep ocean (>4000 m). A detailed description of HYCOM physics is provided by Bleck (2002). A brief description of the model setup is presented below with emphasis on the numerical aspects that are most relevant to this study. There are no tides, waves, or data assimilation in the numerical simulation. Sea ice is simulated using the HYCOM default energy loan parameterization.

4.2 Model Grids

The regional HYCOM was run on four different horizontal resolutions, 0.08° (1/12.5°), 0.04°, 0.02°, and 0.01°. The bathymetry is derived from 30 arc-second General Bathymetric Chart of the Ocean (GEBCO, https://www.gebco.net) This region has complex topography and the deep basin is more than 4000 m deep (Fig 13a). Doubling horizontal resolution from 0.08° to 0.04° and 0.04° to 0.02° generates significant bathymetry difference along the shelf break (Fig 13b and 13c). The bathymetry difference between 0.02° and 0.01° is less significant (Fig 13d). We also run HYCOM on two different vertical resolutions, 41 and 81 hybrid coordinate layers vertically with potential density referenced to 2000 m.

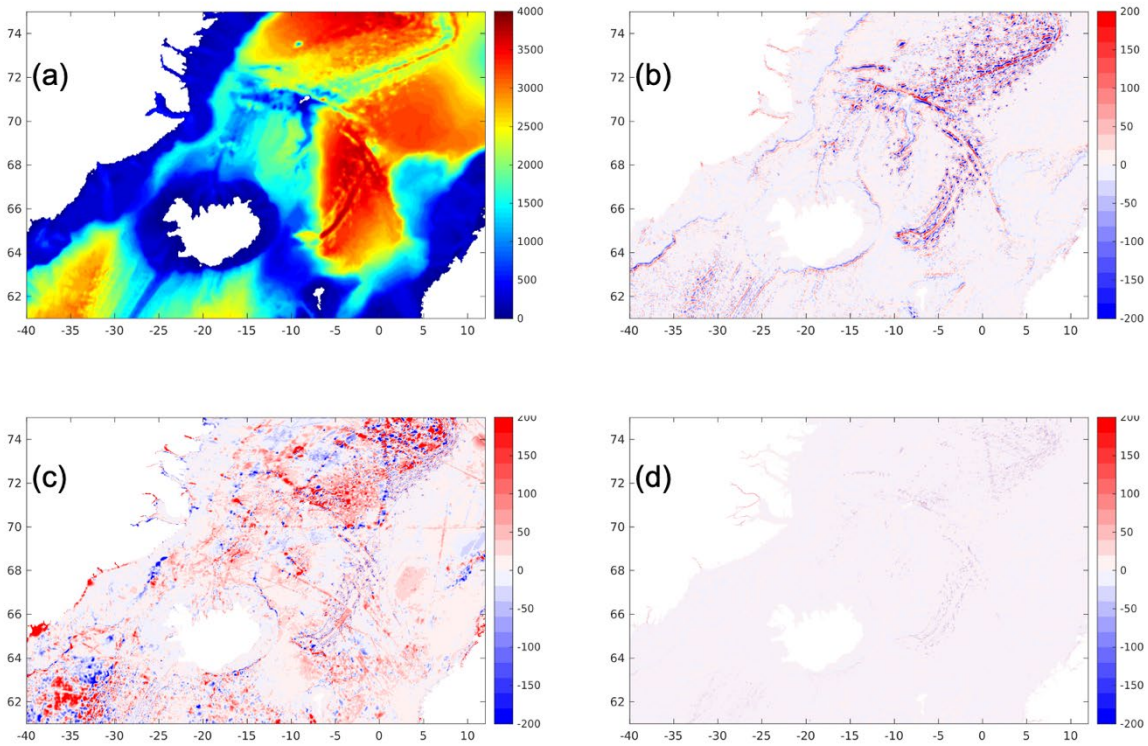

Figure 13 a. HYCOM bathymetry (meters) with 0.08° horizontal resolution. B. HYCOM bathymetry difference (meters) between 0.08° and 0.04° horizontal resolution (0.04°-0.08°). c. HYCOM bathymetry difference between 0.02° and 0.04° horizontal resolution (0.02°-0.04°). d. HYCOM bathymetry difference between 0.02° and 0.01° resolution (0.01°-0.02°).

4.3 Surface Forcing

The HYCOM simulation uses atmospheric forcing from 0.205° hourly NCEP Climate Forecast System version 2 (Saha et al., 2014). The wind stress formulation in the model includes the ocean surface currents (Yu et al., 2017). The NCEP 10-m wind velocities are read by HYCOM and the wind stress is calculated at every time step, taking into account the ocean surface currents as shown below.

$$\boldsymbol{\tau} = \rho_{air} C_d |\boldsymbol{V_{10}} - \boldsymbol{V_o}| (\boldsymbol{V_{10}} - \boldsymbol{V_o}),$$

where ρ_{air} is the air density at sea level, C_d is the drag coefficient, $\boldsymbol{V_{10}}$ is the 10-m wind velocity and $\boldsymbol{V_0}$ is the velocity of ocean surface currents at 1 m depth.

4.4 Initialization and boundary conditions

The initialization state comes from a global HYCOM reanalysis (73X series) with 0.08° horizontal resolution and 41 vertical hybrid layers. Along the open boundary, the boundary conditions include two parts: barotropic (depth averaged) and baroclinic (three dimensional) boundary conditions, from the same global HYCOM reanalysis. The barotropic components are based on Browning and Kreiss (1982, and 1986). The baroclinic boundary condition is applied via relaxation in a buffer zone within 10 outer grid points. For the 81 vertical hybrid layer cases, initial states and open boundary conditions are remapped from 41 to 81 layers.

4.5 Model results from simulations with 41 layers

These HYCOM simulations are run from 12 Z on August 1, 2017 for 28 days except the ones with 0.01° horizontal resolutions. The 0.01° HYCOM is extremely computationally expensive. It takes three days to finish a five-day simulation with 1488 cpus on Gaffney.

The five-day forecast Sea Surface Height (SSH) fields from HYCOM simulations with 41 vertical layers are shown in Figure 14. Figure 14a is the result from HYCOM simulations with 0.08° horizontal resolution. Doubling horizontal resolution from 0.08° to 0.04° (Fig. 2b) and 0.04° to 0.02° (Fig. 14c) generates more SSH difference in the shallower region and along the shelf break than the difference between 0.02° and 0.01° horizontal resolution (Fig. 14d).

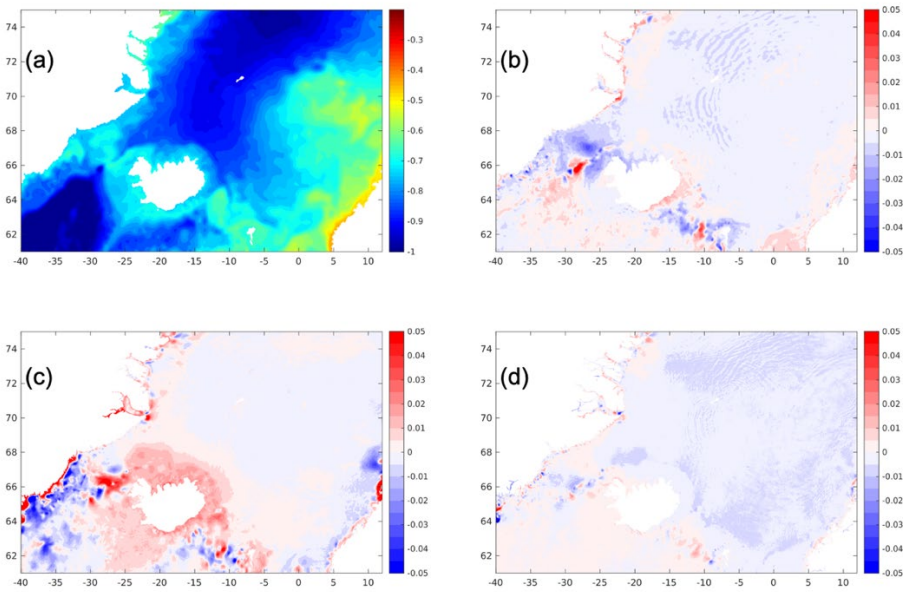

Figure 14 a. HYCOM SSH (m) with 0.08° horizontal resolution; b. HYCOM SSH difference (m) between 0.08° and 0.04° horizontal resolution (0.04°-0.08°); c. HYCOM SSH difference (m) between 0.02° and 0.04° horizontal resolution (0.02°-0.04°); and d. HYCOM SSH difference between 0.02° and 0.01° horizontal resolution (0.01°-0.02°) at 12Z on August 6, 2017. All simulations are run with 41 layers.

The five-day forecast Sea Surface Temperature (SST) fields from HYCOM simulations with 41 vertical layers are shown in Figure 3. The results clearly indicate the warm water from Atlantic along the east boundary and cold water mass along Greenland coast (Figure 15a). SST differences by increasing horizontal resolution (Fig. 15b-d) are mainly confined along the coast of Greenland and the DSE front.

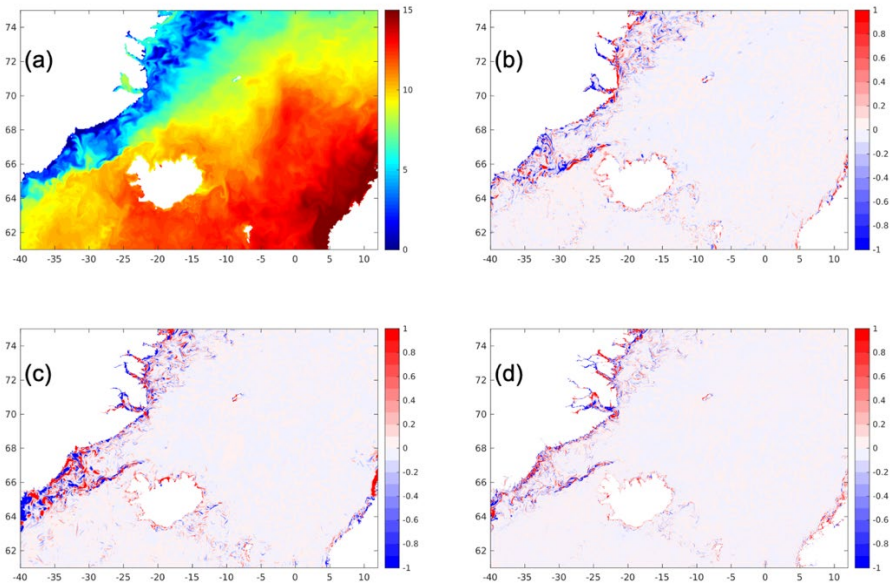

Figure 15 a. HYCOM SST (°C) with 0.08° horizontal resolution; b. HYCOM SST difference between 0.08° and 0.04° horizontal resolution (0.04°-0.08°); c. HYCOM SST difference between 0.02° and 0.04° horizontal resolution (0.02°-0.04°); and d. HYCOM SST difference between 0.02° and 0.01° horizontal resolution (0.01°-0.02°) at 12Z on August 6, 2017. All simulations are run with 41 vertical levels.

4.6 Model results from simulations with 81 layers

These HYCOM simulations are run from 12 Z on August 1, 2017 for 28 days except the 0.01° horizontal resolutions. We didn't run the 81 vertical layer 0.01° HYCOM simulation since it's so computational expensive. SSH and SST from 0.08° HYCOM simulations are shown below as examples. Results from 0.04° and 0.02° HYCOM simulations are similar.

The five-day and 28-day SSH forecast from the 41-layer HYCOM simulation are shown in Figure 16a and 16c, respectively. The five-day and 28-day SSH forecast difference between the 81-layer and 41-layer HYCOM simulations, defined as the SSH from 81-layer simulation minus that from 41-layer simulation, are shown in Figure 16b and 16d, respectively. The results indicate that increasing the vertical resolution decreases SSH around Iceland. And the most SSH difference are around and south of Iceland. This is different than increasing the horizontal resolution where SSH increases around Iceland (Fig. 14b-14d).

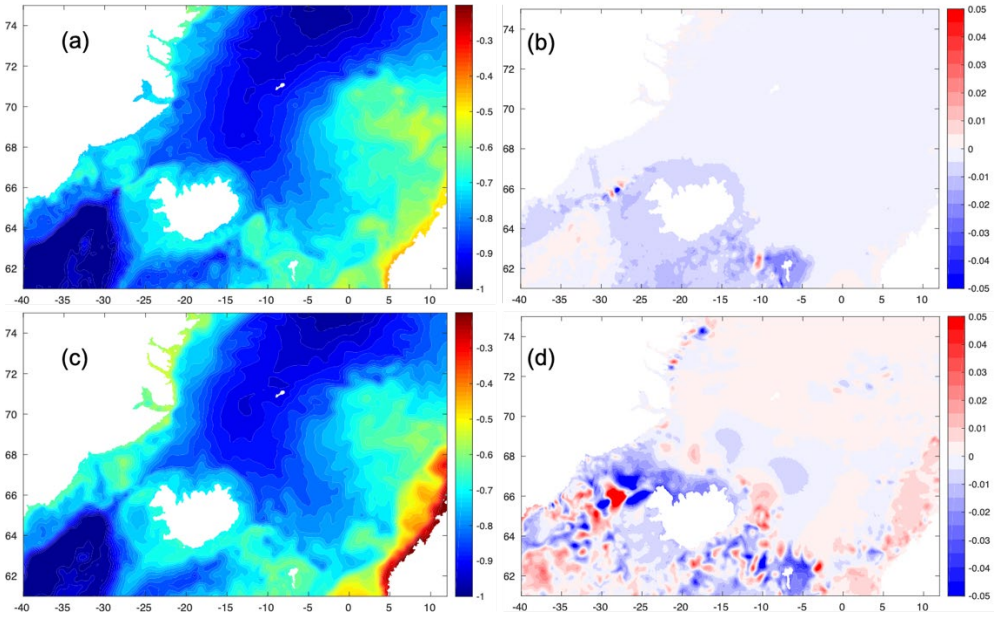

Figure 16 The simulated HYCOM SSH (m) with 0.08° horizontal resolution at 12Z on a. August 6, 2017 and c. August 29, 2017 and the HYCOM SSH difference (m) between 81 and 41 vertical hybrid layers (81L-41L) at 12Z on b. August 6, 2017 and d. Augsut 29, 2017.

Figure 17 is the same as Figure 16 except for SST instead of SSH. Increased vertical resolution has a broad warming effect (Figure 17b and 17c). The maximum SST difference is along the DSE front, which agrees with the effect of increasing horizontal resolution.

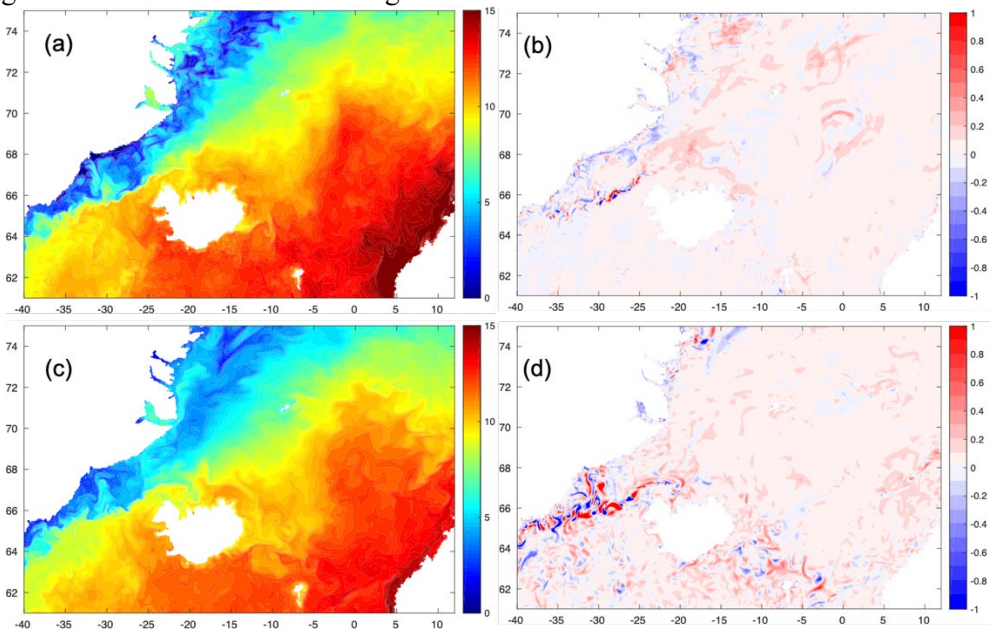

Figure 17 The simulated HYCOM SST (°C) with 0.08° horizontal resolution at 12Z on a. August 6, 2017 and c. August 29, 2017 and the HYCOM SST difference (°C) between 81 and 41 vertical hybrid layers (81L-41L) at 12Z on b. August 6, 2017 and d. Augsut 29, 2017

4.7 Statistics

Hourly SSH and SST results from HYCOM simulations are also compared with the global reanalysis (73X) results. We calculate three statistics to show the agreement between the regional simulation and reanalysis. The first one is the correlation coefficient between HYCOM simulation and global reanalysis. The correlation coefficient indicates how well the spatial pattern agree with each other. The second is the standard deviation of the difference between HYCOM simulation and global reanalysis. This tells us the magnitude difference between the forecasts and the reanalysis. The third is the mean of the difference between HYCOM simulation and global reanalysis. This indicates the broad change of the field.

We first present the impact of the horizontal resolution on these statistics using results from 41 vertical layer HYCOM simulations. The HYCOM SSH (Figure 18) and SST (Figure 19) forecasts are highly correlated with the global reanalysis results, indicating HYCOM simulations reproduce the spatial distribution of the SSH and SST well. Both correlation coefficients decrease with time, are significant to 99% significance level and more than 0.9. The time average of these time series are summarized in table 1. Overall, increasing horizontal resolution slightly decreases correlation coefficient.

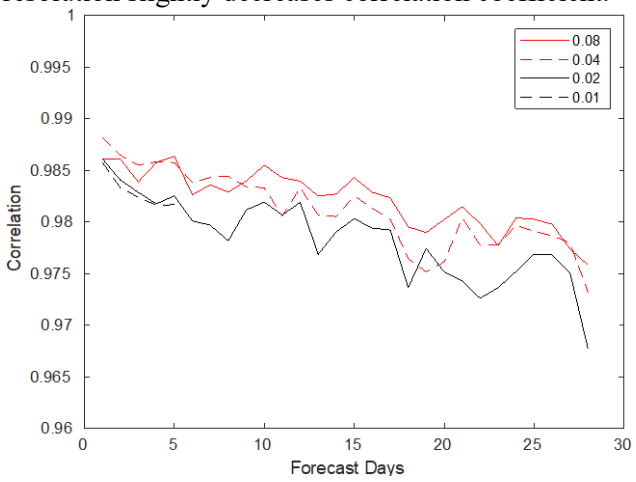

Figure 18. The SSH correlation coefficient between the HYCOM simulations and the global reanalysis. All these simulations have 41 vertical layers.

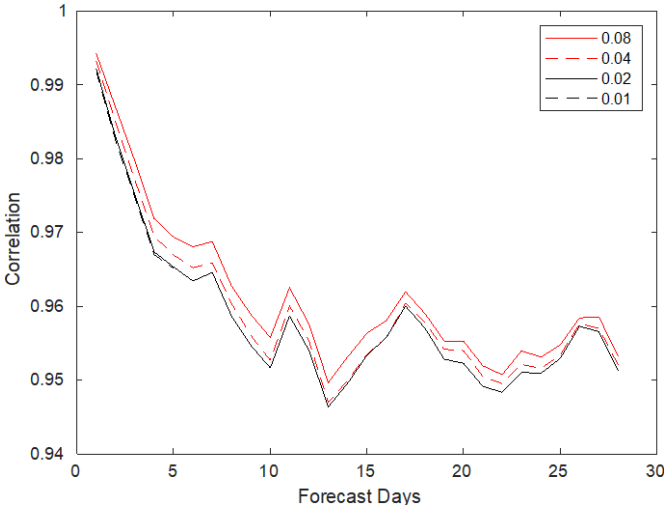

Figure 19. The SST correlation coefficient between the HYCOM simulations and the global reanalysis. All these simulations have 41 vertical layers.

The standard deviation of the SSH (Figure 20) and SST (Figure 21) difference between HYCOM simulations and the global reanalysis increases with forecast time. The SSH difference standard deviation increases from 2 cm in one-day forecast to about 3 cm in 28-day forecast (Figure 20). The SSH difference standard deviation increases from 0.4 ºC in one-day forecast to about 0.9 ºC in 28-day forecast (Figure 21). Increasing horizontal resolution increases the standard deviation slightly.

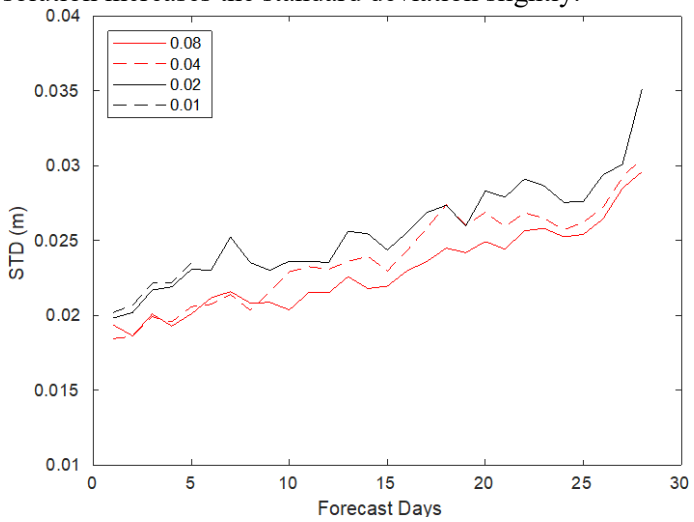

Figure 20. The standard deviation of the SSH difference (meters) between the HYCOM simulations and the global reanalysis. All these simulations have 41 vertical layers.

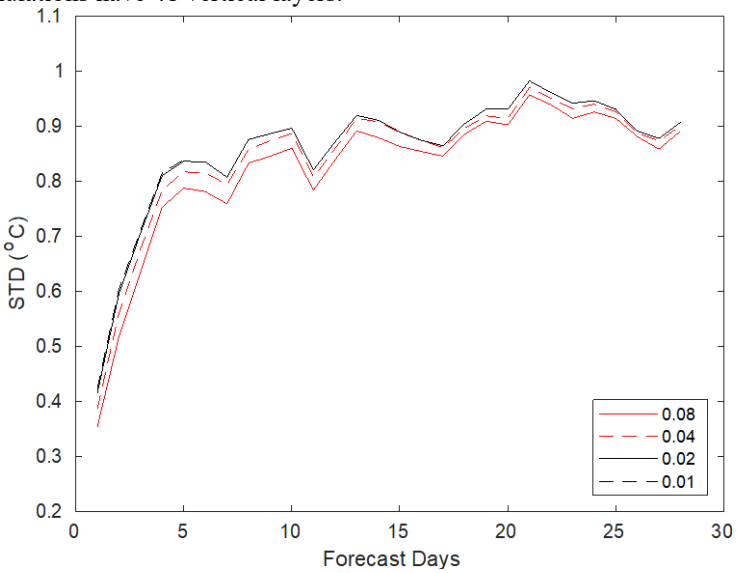

Figure 21. The standard deviation of the SST difference (ºC) between the HYCOM simulations and the global reanalysis. All these simulations have 41 vertical layers.

Figure 22 shows the mean SSH difference between HYCOM simulations and the global reanalysis. Overall, increasing spatial resolution decreases the mean SSH difference. And for SST (Figure 23), the horizontal resolution doesn't change mean SST difference much.

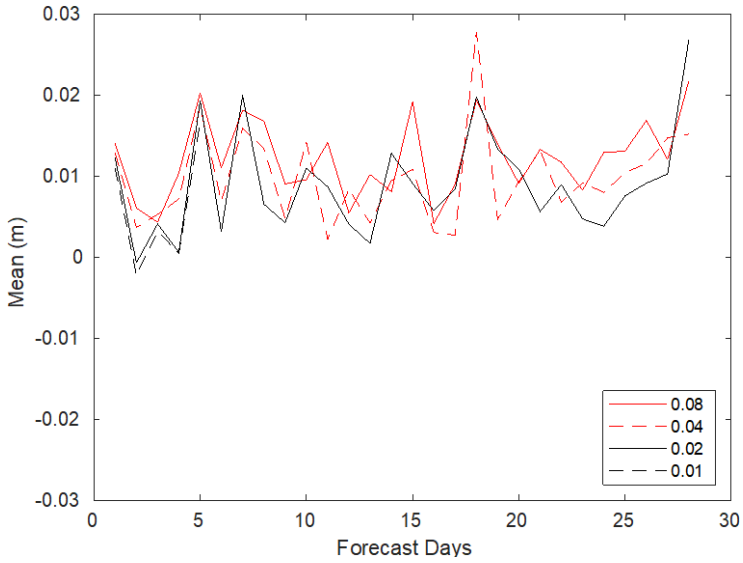

Figure 22. The mean of the SSH difference (meters) between the HYCOM simulations and the global reanalysis. All these simulations have 41 vertical layers.

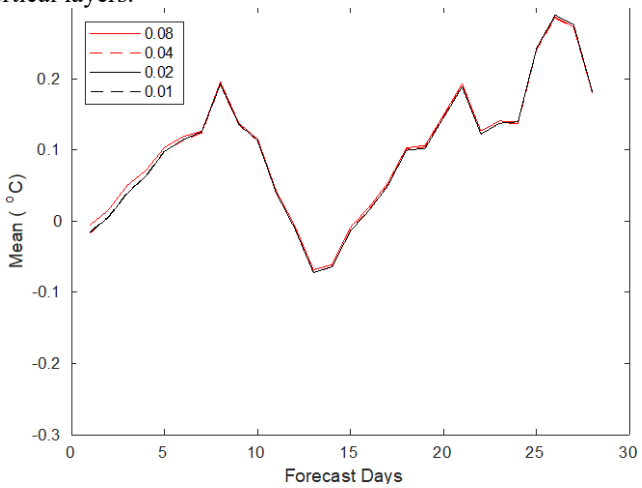

Figure 23. The mean of the SST difference (°C) between the HYCOM simulations and the global reanalysis. All these simulations have 41 vertical layers.

At first glance, one might conclude that increasing horizontal resolution decreases the model performance from Figure 18 to 23. But these differences are not statistically significant as they are well within one standard deviation of these time series. The statistics from the 81 vertical layer forecasts are very similar to those from the 41-layer cases and the time averages are also summarized in Table 1. The differences between them are also less than one standard deviation of the corresponding time series. So statistically, increase horizontal and vertical resolution don't statistically worsen the model forecasts.

Table 1. Time average of the correlation coefficient (correlation) between the forecasts and global reanalysis, the standard deviation (std) and the area average (mean) of the SSH and SST difference between the forecasts and global reanalysis. The 41L and 81L indicate the 41 and 81 vertical layers. Please note that there are no 81 vertical layer forecasts with 0.01° horizontal resolution and only five days 41 vertical layer forecasts.

horizontal resolution			0.08	0.04	0.02	0.01
SSH	correlation	41L	0.98	0.98	0.98	0.98
		81L	0.98	0.98	0.98	
	std (cm)	41L	2.3	2.4	2.6	2.2
		81L	2.3	2.5	2.6	

	mean (cm)	41L	1.1	0.9	0.8	0.5
		81L	0.8	0.5	0.4	
SST	correlation	41L	0.96	0.96	0.96	0.98
		81L	0.96	0.96	0.96	
	std (°C)	41L	0.81	0.83	0.84	0.61
		81L	0.81	0.83	0.85	
	mean (x10^{-1} °C)	41L	0.84	0.82	0.82	0.09
		81L	1.13	1.05	1.06	

4.8 Comparing with VIIRs

An eight-day (August 13 to 20, 2017) SST composite from the NASA Visible Infrared Imaging Radiometer Suite (VIIRS) is shown in Figure 24. The eight-day time average of the HYCOM forecasts are used to compare with the VIIRS data. The SST difference between the HYCOM forecasts with 41 vertical layer and 0.08° horizontal resolution and VIIRS is shown in Figure 25 as an example. Forecasts are warmer along Greenland coast, north of Iceland and eastward to the Norwegian coast (Figure 25) and cooler to the south of Iceland than VIIRS. The model fields are highly correlated with VIIRS but overall is warmer than observations. The statistics of other forecasts are similar and summarized in Table 2.

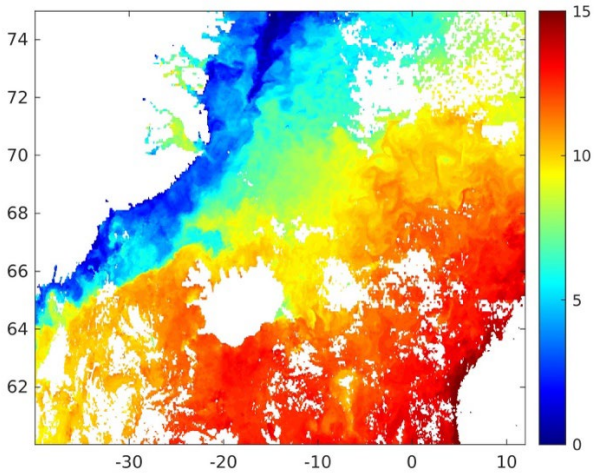

Figure 24. The NASA VIIRS sea surface temperature (°C) during August 13 to 20, 2017.

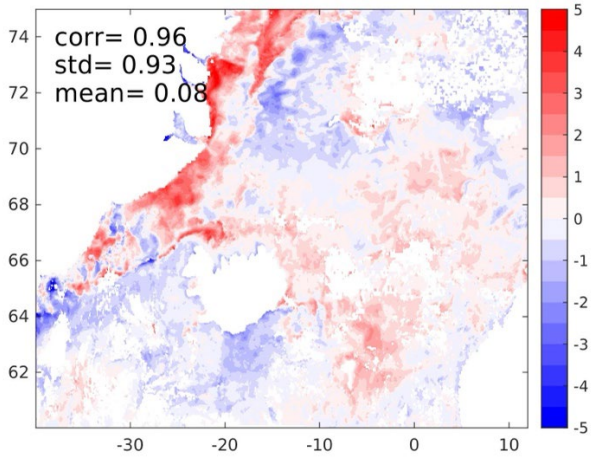

Figure 25. The SST difference (°C) between HYCOM forecasts and VIIRS during August 13 to 20, 2017.

Table 2: The correlation coefficient (correlation) between the forecasts and the VIIRS data, the standard deviation (std) and the area average (mean) of the SST difference between the forecasts and the VIIRS data during August 13 to 20, 2017. The 41L and 81L indicate the 41 and 81 vertical layers.

horizontal resolution			0.08	0.04	0.02
SST	correlation	41L	0.96	0.95	0.95
		81L	0.96	0.95	0.95
	std (°C)	41L	0.93	0.95	0.98
		81L	0.93	0.95	0.99
	mean ($x10^{-1}$ °C)	41L	0.8	0.7	0.6
		81L	1.0	0.9	0.8

5. DEVELOPMENT OF TRACKING ALGORITHM

5.1 Software description

The initial analysis of gradient variability led to an overview and description of frontal variability. An algorithm to provide a connected frontal location in more varied situations required a more disciplined approach. Software was developed on a foundation of C++ code and extended with python code developed within the "Jupyter Notebook" software development environment. Manipulating the data sets using Python within Jupyter Notebook set the stage to use machine learning tools to automate the exploration of the frontal boundaries.

Download scripts were developed to pull data from the NASA Ocean Color Website (https://oceandata.sci.gsfc.nasa.gov). Initially SST and Ocean Color chlorophyll product for 2015 were downloaded and include daily, weekly and monthly composited time ranges. The scripts provided the capability to download other Ocean Color products including water leaving radiance, remote sensing reflectance, turbidity, absorption and scattering products. These data files were stored in the NetCDF format, making them accessible through various NetCDF tools and software libraries. Data for 2015 was downloaded to match and compare with the output from 2015 ocean model runs.

A Python program, "subset_netdf" was developed to open NetCDF files, read and subset the product variable based on a filter of latitude and longitude boundary information and to write the subsetted product variables to an output NetCDF file. Filters defining the latitude and longitude boundaries for the study sites were created, resulting in the ability to extract the products from the global data sets for each of the project's study sites. Therefore, repositories of NetCDF files with data products cropped to the study site extent were built. Subset_netcdf was used to subset SST scenes for the initial study site of the GIUK Gap extent. The resulting subset of the GIUK from the observed SST June 2015 data with locations of the FNMOC "Fronts of Interest" is shown in Figure 26. The color contours of degree Celsius show temperature gradients in the color transitions of blue hues in the colder region and in the yellow and orange hues in the warmer region OFA Fronts of Interest labels (red text) are positioned next to the color transitions of the associated frontal boundary.

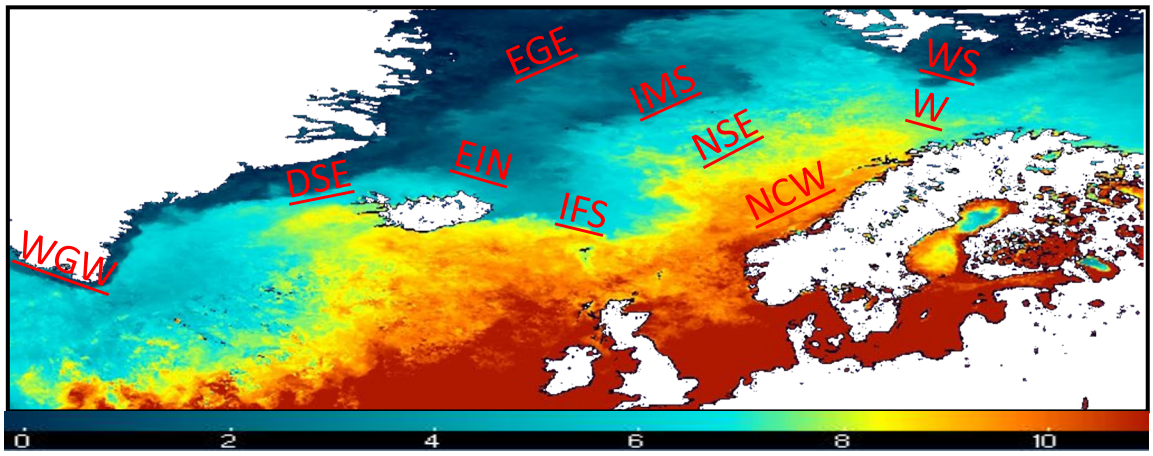

Figure 26. Observed SST for June, 2015 over GIUK after color rescaling

Gradients of the raster data were computed using a variety of different methods. Connecting the pixels of highest value across the raster gradient image were then performed to generate vector information describing the frontal boundary. Therefore, python code was developed to read global products, subset them to the GIUK extent and generate gradient images. An example of the gradient image of the DSE front from the June 2015 Ocean Color SST image with the DSE front in a red bounding box is shown in Figure 27. Several of the FNMOC GIUK "Fronts of Interest" are clearly visible in this image.

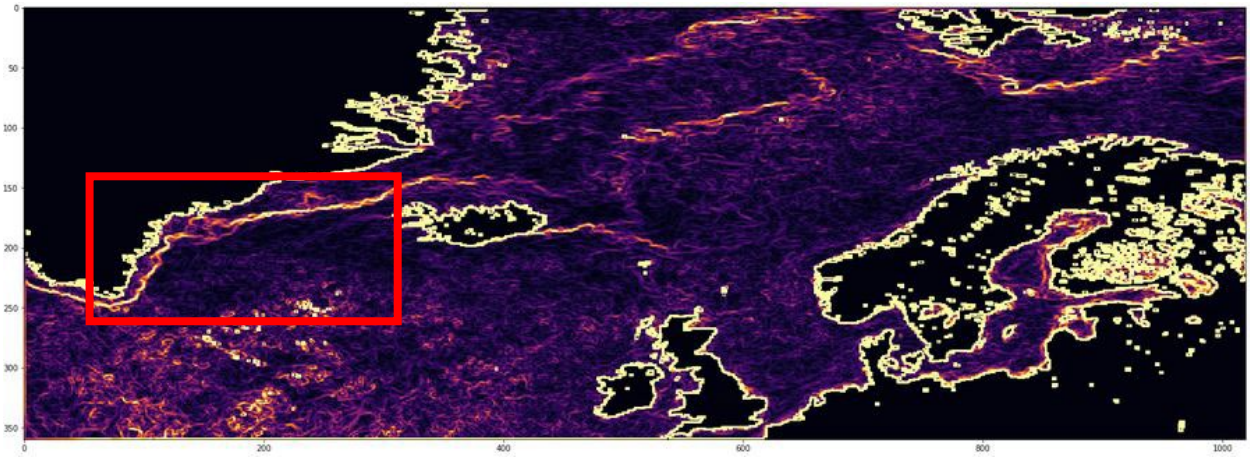

Figure 27. Ocean Color Website SST for June, 2015 over GIUK Gap with DSE front in red bounding box

5.2 Preliminary Frontal Detection Approach

Python code was developed to compute gradient fields from a variety of methodologies, including the Sobel, Prewitt, Laplacian gradient algorithms. The Sobel gradient algorithm being the primary method used. Furthermore, a mask was created over the breadth of the location where the front meanders during a year. The Sobel gradient outside the mask was set to 0 and gradient was copied into the DSE extent. The image in Figure 28 shows the Sobel gradient of the SST over the GIUK extent for June 2015 with the area outside the DSE mask fading to black.

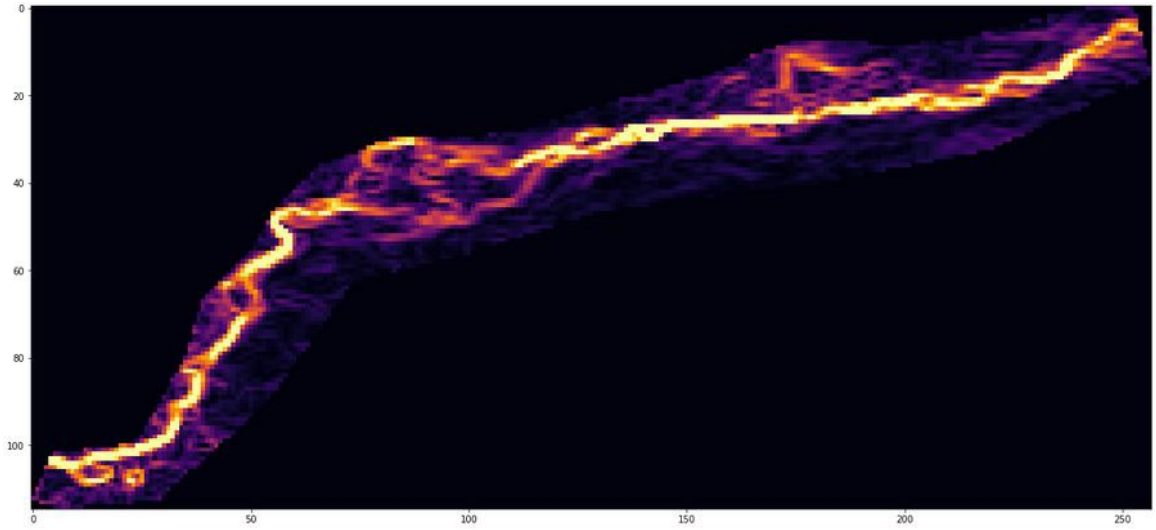

Figure 28. Sobel gradient of the SST over the GIUK extent for June 2015

High gradient values represent sharp change in the raster field, indicating a front. Tracing a line through the path of highest gradient provides a vector depiction of the location of the front. A preliminary approach was performed to generate a vector file of individual point data of <x,y> pairs. This approach located the row of the highest gradient value for each column in the masked area. After these pairs were generated, they were written into a vector file to record the <x,y> points for display. The result of this vector depiction of the SST DSE front based on the Sobel gradient for June 2015 is shown by the blue line in Figure 29.

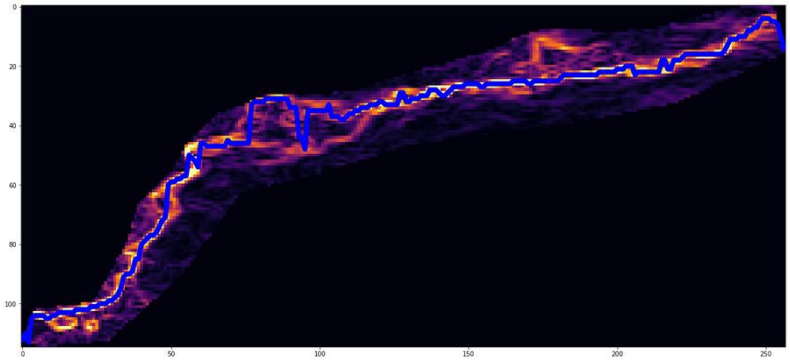

Figure 29. Computed vector depiction of DSE front as blue line in observed June 2015 SST

This approach does not work as well for fronts that have sections with low gradient values between more dominant high gradient values along the front. The selection of appropriate points in the low gradient value regions can be difficult. As an example, the corresponding masked gradient field around the meander for the Iceland-Faroe front for the preliminary front detection approach is shown in Figure 30 (this is for a different date than was used for the above analysis of the DSE). The breadth of possible meanders has a much wider area, and the result in Figure 30b, with its large vertical "jumps", shows the difficulty in using the preliminary approach to connect the appropriate gradient values of the Iceland-Faroe front in the areas that have lower gradient values along the front.

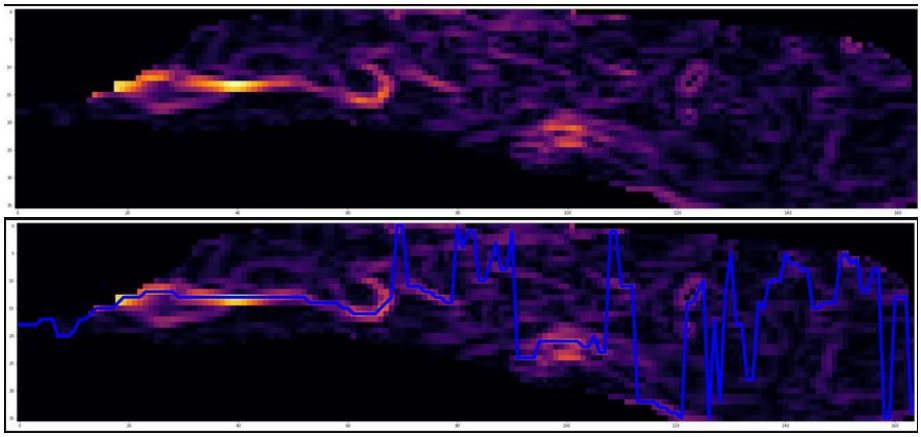

Figure 30. a) Gradient of IFS front for August, 2017, b) preliminary detection method results in blue line

5.3 Search Tree Frontal Detection Approach

The process to download, extract, subset, generate gradients, mask and trace high gradients with the preliminary method was used as a foundation to investigate a more sophisticated gradient tracing algorithm. This approach used a search tree to trace options for high gradient tracing through a raster field. A depiction of a search tree is shown in Figure 31. The leaves represent nodes at gradient pixel location. The branches represent connection to next 5 adjacent nodes (pixels). The tree grows exponentially (powers of 5) as each layer extending away from the original node (pixel location) occurs. For example, third layer already has 25 nodes represented. Therefore, pruning occurs to remove weakly performing paths through the gradient field from the tree. Performance measurements rank highly those paths with high average of gradient values and number of branches. The algorithm uses a data queue to prepare gradient nodes to be inserted into the tree.

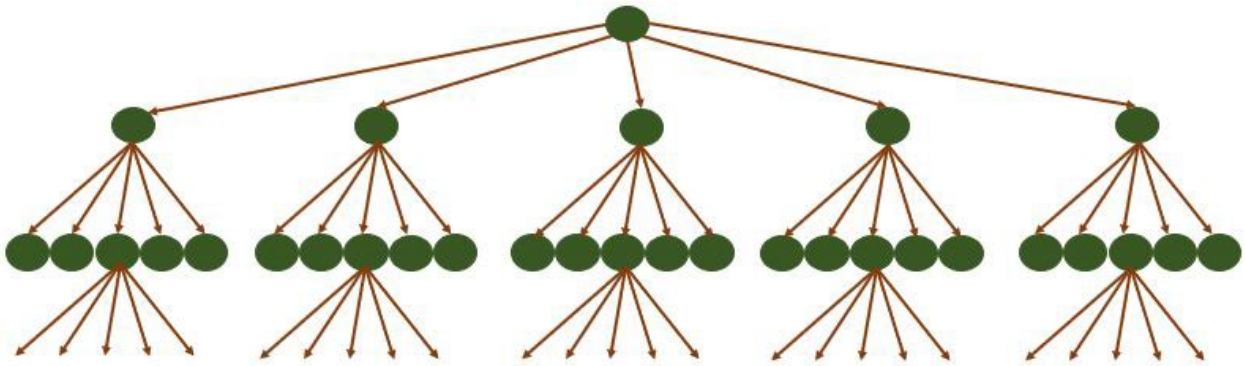

Figure 31. Digital Search Tree: Nodes represent adjacent pixel locations

A basic overview of the Front Line (fline) algorithm is:

- Find first pixel on westernmost side
- Put node information of this pixel in the node's attributes and push it onto the queue
- Pop node from the queue
    - Identify 5 adjacent pixels from the 9 options according to front heading
    - Put node information for these pixels in the node's attributes and push it onto the queue
    - Update performance measurement for node
    - Prune paths that revisit pixels already on tree to prevent infinite looping of path
    - Periodically prune poorly performing paths from tree
    - Stop when no more pixels exist in the queue
- Sort remaining paths according to performance measure
- Write out best paths in xml format and shapefile format

The Sobel gradient for observed SST from August 2017 is shown in Figure 31a. The high gradient values are shown in red, with the middle gradient values in green and the lower gradient values in blue. A path through the raster field can be seen along the lower area of the region with an alternate path separating to the north and then merging again toward the left of the image. As the fline algorithm begins, the left most pixel is found. The paths are identified by traversing adjacent pixels along the heading, initially eastward, and putting these pixel nodes in the queue to be inspected as candidates to include in the search tree. There is a trade-off between pruning and speed of execution, which is still being evaluated.

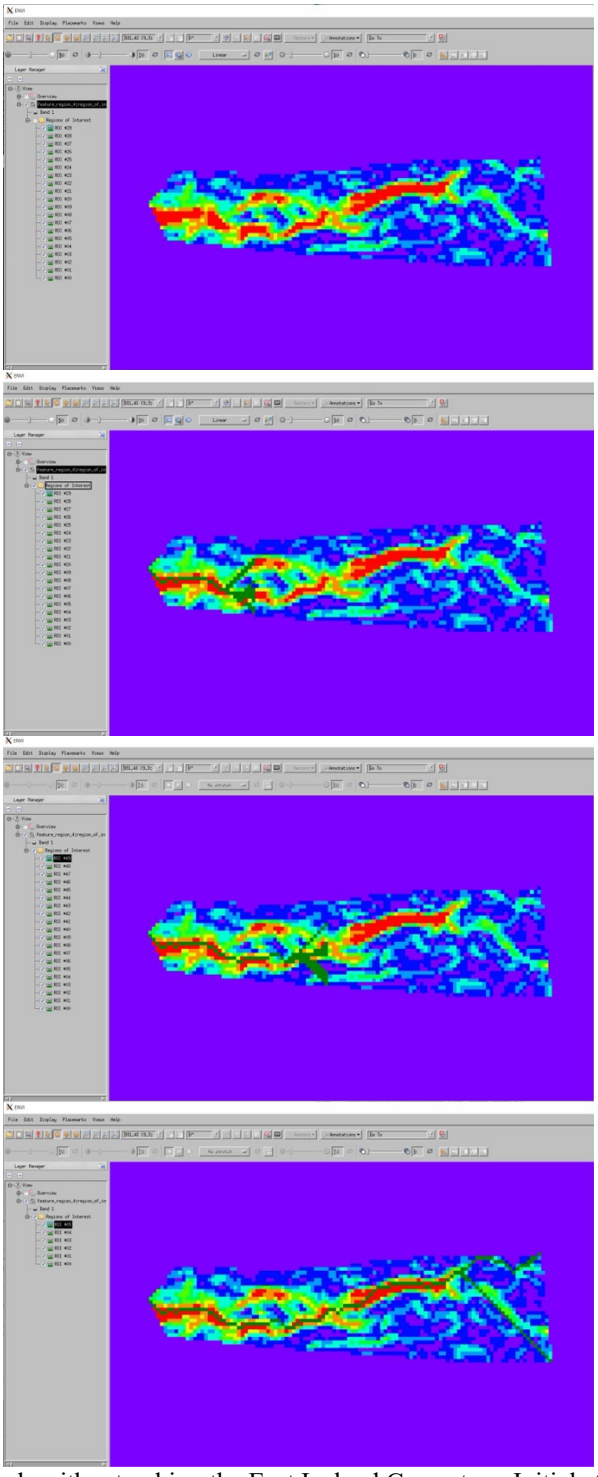

Figure 32: The progress of the algorithm tracking the East Iceland Current. a. Initial state; b. At a depth of about 30; c. at the halfway point; d. complete.

The status as the search tree has a depth of about 30 is shown in Figure 32b. The 20 possible paths are shown in dark green proceeding from the western side toward the east. Initially 2 routes through high gradient path are considered. The top route is weaker gradient path

that separates to the north and then merges again later. The bottom route is through the higher gradient values. Both jump over areas of lower gradient value segments.

Pruning of the tree can be lenient, which increases the run time of the algorithm, or it can be restrictive, which can reduce the run time of the algorithm. Since a component of the algorithm is to prune the search tree from time to time, it is possible to prune out alternate weaker paths through the gradient field. For example, the halfway point of the EIN processing for the June 2017 SST data is shown in Figure 32c. The northern branch of the gradient tracing is not in the top performing routes through the gradient field and may have been pruned out of the tree completely. The performance measure of several tracing option through the southern branch of the gradient field are all higher than the options along the northern branch.

The completion of the gradient tracing for the August 2017 SST is shown in Figure 32d. The green line depicting the "best" solution travels through the southern branch of the high gradient values and then up through the high gradient values that meander northward before turning and following the front to the southeast. The pruning was significant for this run with only 5 routes left from which to pick the "best" option. The entire run took 1 minute and 3 seconds.

More work continued to improve the performance. Various parameters were included in the fline program to control the pruning and execution time. This primarily centered on providing options for the performance measurement function, the allowance of limited sharing of pixels in multiple tracing path options through the raster field and creating jumps across neighborhoods of low gradient values. The work then proceeded to generating vector point data through gradient fields of model and observed data fields on common dates.

The processes to subset, generate and trace gradient fields were performed on the model SST and SSH data for 08/01/15. The image in Figure 33a shows the gradient field from the Modeled SST from 08/01/15 in hues of orange over the IFS front region and the SST front depicted in green. One of the differences in the Modeled and Observed fields, whether they are SST or SSH, is that the Modeled fields have more definition and smaller localized gradient curls. This provides many options for the algorithm tracing to push outside the current high gradient track and into an adjacent high gradient track. Regardless of these dynamics, the fline algorithm results in a "best" option that reasonably traces through the connecting high gradient tracks, skipping over low gradient separations to reconnect with the continuing high gradient track. The "best" option starts along the west coast of Iceland meandering along the high gradient values then southeast toward the Faroe Islands and then pushing north as it reaches the Faroe Islands. There are alternate paths that could have been taken, with a more easterly path about midway across the region. However, the algorithm's performance function determined this to be the best path. Other options do exist in the other final solutions that were not pruned during the tracing process.

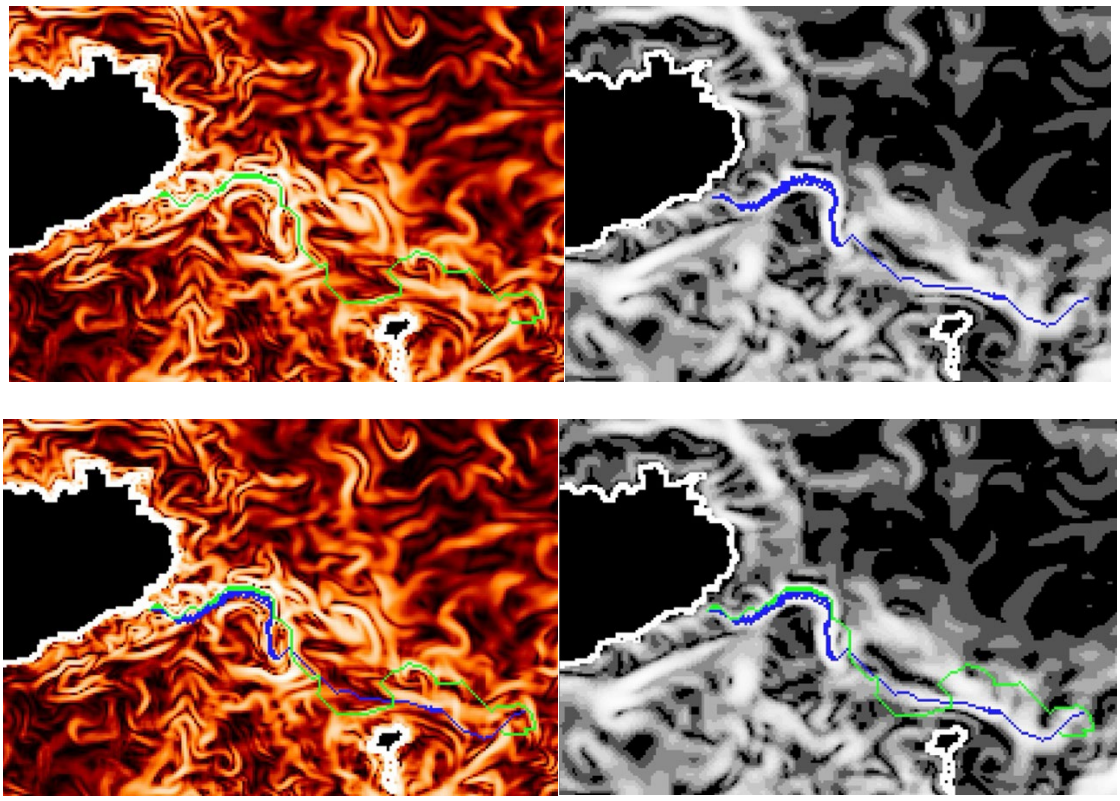

Figure 33: a. Automatically generated SST front, mapped over SST; b. Automatically generated SSH front, mapped over SSH; c. Both SST front (green) and SSH front (blue), mapped over SST; d. Both SST (green) and SSH (blue) fronts, mapped over SSH.

The gradient tracing for the SSH from the same date and time is shown in Figure 33b with the gradient field from the modeled SSH from 08/01/15 in gray shades over the IFS front region and the SSH front depicted in blue. The modeled SSH gradient tracks are more pronounced and dominant than the modeled SST tracks. This results in broad high gradient tracks that cause the tracing to work back and forth along the high gradient ridge. Regardless of this, the approach identifies and traces the southern high gradient track as it runs eastward from Iceland to just north of the Faroe Islands.

These modeled SST and SSH fronts are shown together in Figure 33c with the SST front depicted in green and the SSH front depicted in blue. The background raster image is the Modeled SST grid. The green line depicting SST front runs north of the SSH front as it leaves Iceland then crosses to the south of the SSH front until they cross again just north of the Faroe Islands.

Finally, the modeled SST and SSH fronts are shown again in Figure 33d, this time over the modeled SSH raster field. This shows the SST front in green and its relationship to both the gray-scale SSH raster image with the SSH front boundary in blue.

5.4 Frontal Detection Algorithm Summary

The fline program is modular and broken into several separate function files. Many of the computational issues with search tree have been resolved. Logging from different functions can be turned on and off with flag in the header file. Pruning nodes up and down the tree have been updated to remove dead branches. Traversing methods have been modified to include only gradients values over a preset threshold. Front lines through the gradient field identify multiple high gradient lines of which the performance measurement function is used to select the best performing paths through the data.

As this work proceeds to transition phase, there are some refinements that can be pursued. The final tree search can result in many front-line options and finding the optimal line(s) still needs to be perfected. One option is to continue implementing stricter pruning approaches. The local performance metric for traversal and the global performance metric to select the optimal lines can be updated. The final front options can be written to xml and shapefile formats. Automated approaches for creating the mask file of a particular front's meander region have been developed.

6. COMBINATIONS OF ALGORITHMS

In addition to the work described above to develop an independent frontal tracking algorithm, we needed to determine how best to combine frontal representations from different variables. This investigation of front detection methods and observational and model representations focused again on the Iceland-Faroe Front. The time frame selected was August of 2017, based on the availability and coverage of Satellite VIIRS-SNPP 8 days composites of SSTs and Chl.

As this analysis was performed while the automated algorithm was still under development, we used a Matlab routine called "edge" to estimate the location of the Iceland-Faroe front in the HYCOM model surface fields (SST, SSH, SSS, surface currents magnitudes), as well as in satellite VIIRS observations of SST and CHL. The well-known Sobel method was used to estimate the locations of the front in different products. The Sobel method determines areas suspected to be frontal structures based on the magnitudes of the image's gradient. The "edge" routine uses a threshold, and determines frontal structures in areas where the gradient magnitudes are larger than the threshold. Users can specify the value of threshold, or the edge routine will automatically generate one (this is called auto-threshold; the selection of an auto-threshold is based on estimated noise to signal ratio). We proposed our own estimation of an optimal threshold, based on the mean and standard deviation of the gradient field of the specific field (HYCOM model surface fields or satellite observations). In our approach, the threshold is equal to the mean value of the gradient plus three standard deviations of the gradient field. Comparisons show that thresholds estimated by our approach are mostly higher than those provided by Matlab auto-thresholds.

Figure 34 shows HYCOM SST fields averaged over 8 days (20170813-20170820). The location of the IFS front (determined by the Sobel method) is shown as a black solid line on the Figure 34. Figure 35 shows VIIRS 8 days (20170813-20170820) composite of SST field. The

location of the IFS front (also determined by the Sobel method) is shown as a black solid line. In spite of the fact that SSTs from multiple satellites (including VIIRS) were assimilated into the HYCOM, there are distinct differences in locations of the IFS front determined from the satellite and the model data.

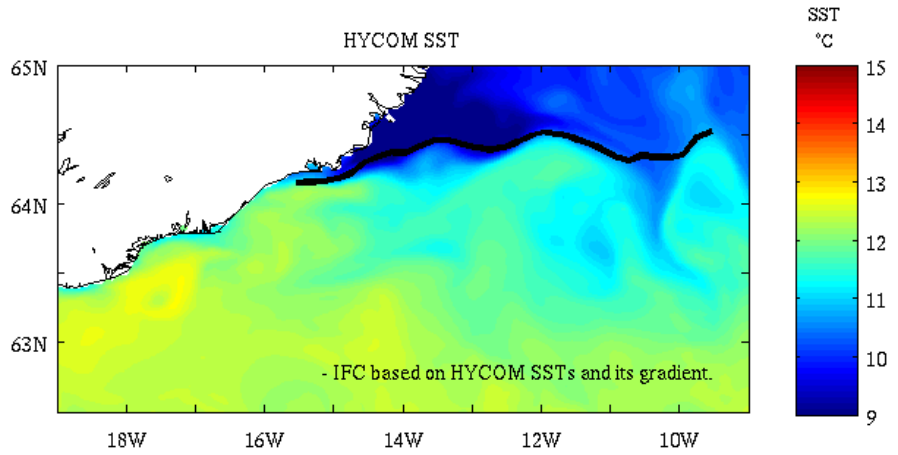

Figure 34. HYCOM SST fields averaged over 8 days (20170813-20170820). The location of the IFS front is shown as a black solid line.

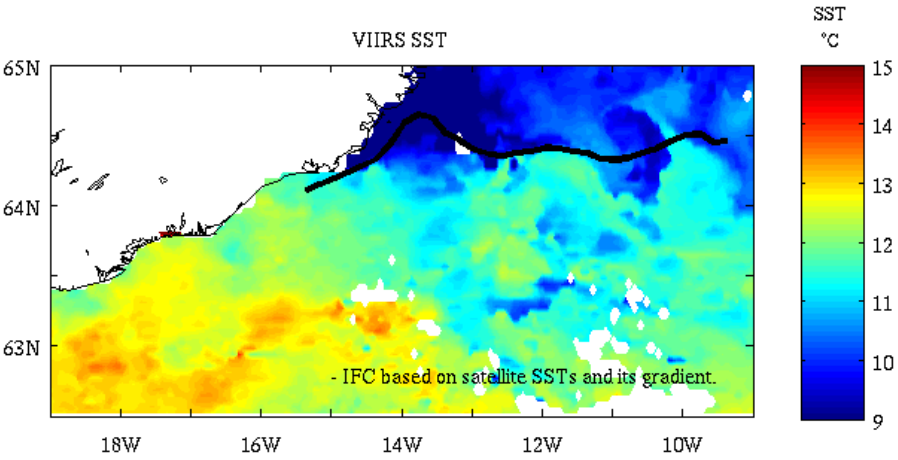

Figure 35. 8 days composite (20170813-20170820) of VIIRS SST field. The location of the IFS front is shown as a black solid line.

The question we have addressed in this investigation is what is the best way to merge information from the model predictions (SST, SSH, SSS, surface currents magnitudes) and observations in order to estimate the optimal location of the front? We have developed a variational approach to combine together frontal representations from different products, like for example from the model and observed SSTs on Figures 34 and 35, and to provide the optimal location of the front. The variational approach minimizes a cost function representing a sum of the misfits between optimal front location and front locations from different products. Misfits in the cost function are weighted by their respective ratios of the corresponding field values to its gradients. As a result of the cost function minimization, the optimal front location is close to the locations where changes in the field values are large relative to surrounding points, and far away

from locations where changes in the field value are small relative to surrounding points (for example, the field value is large but gradient is small). Figure 36 shows the optimal location of the IFS front based on the application of the variational approach to two IFS front representations in the model and satellite SSTs (from Figures 34 and 35).

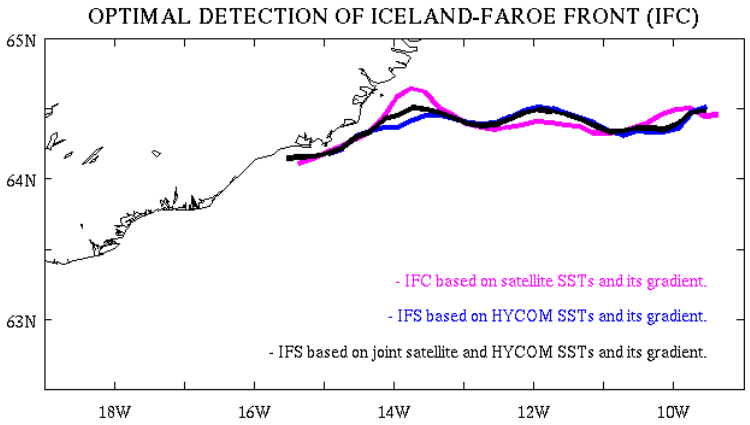

Figure 36. Optimal location of the IFS front (black line) determined by the variational approach.

We have found weak representations of IFS in the VIIRS Chl field and in the VIIRS log10 transformed Chl fields when we used the Sobel and Canny methods to determine the front location (both methods are provided by the Matlab routine "edge"). We have investigated relations between the IFS front representations in SSTs and Chl fields. Figure 37 shows the VIIRS log 10 transformed 8 days composite (20170813-20170820) of the VIIRS Chl field with the VIIRS SST 8 days composite contours overlay. Based on Figures 35 and Figure 37, high values of Chl are on the warmer side of the front, thus indicating that phytoplankton bloom is located on the warmer side of the IFS front. This will lead to increase of the temperature gradient across the IFS front and intensification of the strength of the front due to trapping the atmospheric heat from the short wave radiation by the phytoplankton on the warmer side of the IFS front.

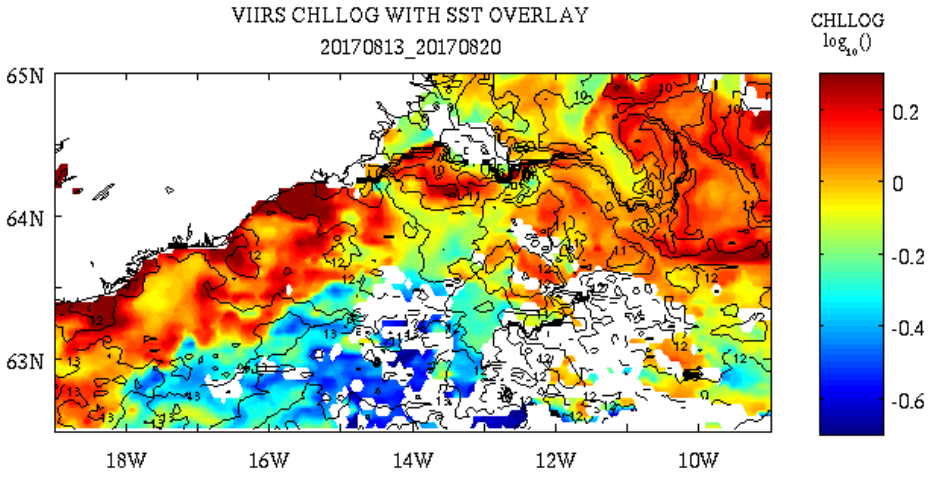

Figure 37. The VIIRS log 10 transformed 8 days composite (20170813-20170820) of the VIIRS Chl field with the contours of the VIIRS SST 8 days composite overlay.

7. CONCLUSIONS

This report includes many of the results of the Feature Location and Variability project. Collectively, these results will be used to develop and implement an operational, automated frontal detection algorithm. The results described in the first section will provide the "envelope" necessary for providing bounds to the frontal algorithm, so that the frontal-tree detection approach has the limits that make it a viable, computationally feasible tool. The modeling analysis sharpens our understanding of the improvements that may come as higher resolution model output becomes available, and also demonstrates that improvements become negligible for analyses that focus on the scales that are important to us at this time. The algorithm itself, while requiring some further development and testing to ensure that it is robust for all locations, will provide the basis for the operational tool necessary. This work has already been funded through an NRL 6.4 proposal. Finally, the tools used to combine analysis from different variables will ensure that rather than focus on only one variable, we can provide a frontal location that includes input from all sources and gives a comprehensive assessment of what variables are changing, where they are changing, and what changes are most relevant to the warfighter in real time.

REFERENCES

1. Bleck, R., 2002: An oceanic general circulation model framed in hybrid isopycnic-Cartesian coordinates. Ocean Model., 4, 55-88
2. Browning, G., and H.-O. Kreiss, 1982: Initialization of the shallow water equations with open boundaries by the bounded derivative method. Tellus, 34, 334-351.
3. Browning, G., and H.-O. Kreiss, 1986: Scaling and computation of smooth atmospheric motions. Tellus, 38A, 295-313.
4. Chassignet, E.P., L.T. Smith, G.R. Halliwell, and R. Bleck, 2003: North Atlantic simulations with the Hybrid Coordinate Ocean Model (HYCOM): Impact of the vertical coordinate choice, reference pressure, and thermobaricity. J. Phys. Oceanogr., 33, 2504-2526.
5. Metzger, E. J., O. M. Smedstad, P. G. Thoppil, H. E. Hurlburt, J. A. Cummings, A. J. Wallcraft, L. Zamudio, D. S. Franklin, P. G. Posey, M. W. Phelps, P. J. Hogan, F. L. Bub, and C. J. Dehaan, 2014. US Navy Operational Global Ocean and Arctic ice prediction systems. Oceanogr., 27, 32-43.
6. Saha, S., and Coauthors, 2014: The NCEP Climate Forecast System version 2. J. Clim., 27, 2185-2208. Doi:10.1175/JCLI-D-12-00823.1.
7. Walton, C.C., W. G. Pichel, and J.F. Sapper, The development and operational application of nonlinear algorithms for the measurement of sea surface temperatures with the NOAA polar-orbiting environmental satellites, Journal of Geophysical Research, Vol. 103, No. C12, Pg 27,999-28.012, November 15, 1998
8. Yu, Z., E. J. Metzger, and Y. Fan, 2017: The impact of ocean surface currents on Sverdrup transport in the midlatitude north Pacific via the wind stress formulation. J. Phys. Oceanogr., 47, DOI:10.1175/JPO-D-16-0155.1.